Research Square

Preprints are preliminary reports that have not undergone peer review.
They should not be considered conclusive, used to inform clinical practice,
or referenced by the media as validated information.

# Projected Warming and Extreme Precipitation Changes across the Himalayan Arc Using WRF Regional Climate Simulations

**KULDEEP SHARMA**

kuldeep.nihr@gov.in

National Institute of Hydrology https://orcid.org/0000-0001-9403-0988

**Vishal Singh**
National Institute of Hydrology

**Deepak Singh Bisht**
National Institute of Hydrology

**Somesh Kumar**
National Institute of Hydrology

**Sahidul Islam**
Centre for Development of Advanced Computing

**Mohammad Sajeed**
Centre for Development of Advanced Computing

**Ramesh Bulusu**
Centre for Development of Advanced Computing

**Research Article**

**Keywords:** Himalaya, WRF dynamical downscaling, CMIP6 projections, Elevation-dependent warming, Extreme precipitation, climate change

**Posted Date:** June 10th, 2026

**DOI:** https://doi.org/10.21203/rs.3.rs-9650448/v1

**License:** This work is licensed under a Creative Commons Attribution 4.0 International License.
Read Full License

**Version of Record:** A version of this preprint was published at Climate Dynamics on October 23rd, 2026.
See the published version at https://doi.org/10.1007/s00382-026-08442-3.

# Projected Warming and Extreme Precipitation Changes across the Himalayan Arc Using WRF Regional Climate Simulations

Kuldeep Sharma[1]*, Vishal Singh[1], Deepak Singh Bisht[1], Somesh Kumar[1], Sahidul Islam[2]
Mohammad Sajeed[3], Ramesh Bulusu[3]

*Corresponding Author

[1]Centre for Cryosphere and Climate Change Studies, National Institute of Hydrology, Roorkee

[2]HPC-ESEG Group, Centre for Development of Advanced Computing (CDAC), Pune, India

[3]HPC Technologies Group, Centre for Development of Advanced Computing (CDAC), Pune, India

## Abstract

The Himalayan region is highly vulnerable to climate change due to its complex topography, strong elevation gradients, and interactions between monsoonal and extratropical circulation systems, which remain inadequately resolved in coarse-resolution global climate models. To address this issue, this study uses high-resolution (9 km) dynamical downscaling with the Weather Research and Forecasting (WRF) model, driven by bias-adjusted Max Planck Institute Earth System Model (MPI-ESM-HR) participating in the Coupled Model Intercomparison Project Phase 6 (CMIP6) simulations, to assess the projected changes in temperature, precipitation, and extreme precipitation across the Western, Central, and Eastern Himalaya under SSP2-4.5 and SSP5-8.5 scenarios. Model evaluation against multiple observational and reanalysis datasets demonstrates good agreement in reproducing historical spatial patterns, seasonal variability, and elevation-dependent temperature gradients across the Himalayan region. Results indicate widespread warming across the Himalaya during 2031–2060, with temperature increases of approximately 1–2°C under Shared Socioeconomic Pathway 2-4.5 (SSP2-4.5) and 2–4°C under Shared Socioeconomic Pathway 5-8.5 (SSP5-8.5), with stronger warming at higher elevations and over the northern Himalayan ranges. Precipitation projections show strong spatial and seasonal heterogeneity. Annual precipitation increases by approximately 10–40% during the near-future period (2031-2045) across parts of the western and central Himalaya, while late-future (2046-2060) changes become more spatially heterogeneous, with precipitation decreases of nearly 10–20% over parts of Himachal Pradesh, Uttarakhand, and adjoining plains. Results further show that extreme precipitation intensifies despite spatially heterogeneous changes in mean precipitation. Rx1day and Rx5day increase by approximately 5–15 mm, with localized increases exceeding 15 mm under SSP5-8.5. The frequency of extreme precipitation events increases by 2–6 days $yr^{-1}$, while their contribution to annual precipitation rises by approximately 2–10%, particularly across the Western Himalaya and mid-elevation zones. These findings highlight strong regional and elevation-dependent hydroclimatic changes and demonstrate the value of high-resolution dynamical downscaling for improving future climate risk assessments at fine spatial scales across the Himalayan region.



**Keywords:** Himalaya; WRF dynamical downscaling; CMIP6 projections; Elevation-dependent warming; Extreme precipitation; climate change

## 1. Introduction

The Himalayan region is one of the most climatically sensitive and hydrologically critical mountain systems on Earth, often referred to as the "Water Tower of Asia" due to its role in sustaining major river basins such as the Indus, Ganges, and Brahmaputra (Immerzeel et al., 2010; Pritchard, 2019). The region is characterised by complex topography, strong elevation gradients, and the interaction of multiple large-scale circulation systems, including the South Asian summer monsoon and wintertime extratropical disturbances. These interactions generate pronounced spatial variability in temperature and precipitation across the Himalayan arc, making the regional hydroclimate highly sensitive to ongoing anthropogenic climate change (Bookhagen and Burbank, 2010; Palazzi et al., 2013; Krishnan et al., 2020).

The Himalayan hydroclimate also exhibits strong west–east contrasts. The Western Himalaya receives a substantial fraction of winter (December-February) precipitation from western disturbances and remains comparatively colder and drier, particularly over Ladakh and trans-Himalayan regions. In contrast, the Central and Eastern Himalaya are increasingly influenced by the South Asian summer monsoon, with the Eastern Himalaya receiving higher annual precipitation due to stronger moisture transport from the Bay of Bengal and pronounced orographic uplift. These regional differences strongly influence snow accumulation, glacier mass balance, river discharge seasonality, and downstream water availability across Himalayan catchments. Winter precipitation, in particular, plays a critical role in maintaining seasonal snowpack and glacier recharge across high-elevation basins of the Western Himalaya.

Recent decades have witnessed significant warming across the Himalayan arc, with several studies reporting amplified temperature increases at higher elevations, a phenomenon often termed as elevation-dependent warming (EDW) (Pepin et al., 2015). Such warming has profound implications for cryospheric processes, including glacier mass balance, snow cover dynamics, and the timing of meltwater contributions to downstream river systems (Huss and Hock, 2018; Kraaijenbrink et al., 2017). Concurrently, changes in precipitation patterns, particularly in extreme events, pose substantial risks of floods, landslides, and glacial lake outburst floods (GLOFs), especially in steep and densely populated mountain environments (Dube et al., 2014, Allen et al., 2019; Wester et al., 2019).

Despite substantial advances in global climate modelling, projecting future hydroclimatic changes across the Himalayan region remains challenging because of difficulties in representing complex terrain, orographic precipitation, and fine-scale land–atmosphere

interactions. Coarse-resolution global climate models (GCMs) often inadequately represent orographic precipitation processes, monsoon–terrain interactions, western disturbance activity, and localized precipitation extremes across the Himalaya (Giorgi and Gutowski, 2015; Krishnan et al., 2020; Lee et al., 2022). As a result, regional climate models (RCMs) and dynamical downscaling approaches have increasingly been employed to provide improved representation of fine-scale climatic variability and hydroclimatic extremes over mountainous terrain (Palazzi et al., 2015; Sharma et al., 2021; Singh et al., 2024). High-resolution simulations are particularly important for resolving elevation-dependent hydroclimatic processes and extreme precipitation characteristics, which are often spatially smoothed or underestimated in coarse-resolution GCM outputs. Recent studies further highlight that precipitation responses over the Himalaya exhibit strong spatial heterogeneity and seasonally dependent behaviour associated with variations in monsoon circulation, atmospheric moisture transport, and western disturbance activity (Krishnan et al., 2019; Pattnayak et al., 2023; Pant et al., 2024;Yadav et al., 2024).

Another critical dimension of climate change over the Himalaya is the behaviour of extreme precipitation. Extreme precipitation intensity and frequency have shown increasing trends in both observations and future climate projections, indicating a transition toward more episodic and intense precipitation regime (Fischer and Knutti, 2016; Seneviratne et al., 2021). Indices such as Rx1day, Rx5day, and R95p are particularly important for assessing future hydroclimatic hazards including floods, landslides, and glacier-related risks in steep mountain environments. However, substantial uncertainty remains regarding the spatial distribution, elevation dependence, and temporal evolution of projected extreme precipitation across the Himalayan region, particularly at fine spatial resolution. Existing studies have primarily focused either on mean climate change or selected precipitation extremes, often using relatively coarse-resolution simulations that inadequately resolve fine-scale topographic gradients and regional hydroclimatic contrasts across the Western, Central, and Eastern Himalaya (Dimri et al., 2015; Sanjay et al., 2020; Singh et al., 2024). In particular, the combined behaviour of mean precipitation change, extreme precipitation intensity, event frequency, and their elevation-dependent responses remains insufficiently constrained across the Himalayan region. Addressing these uncertainties is critical for improving assessments of future hydroclimatic risks, water availability, cryospheric response, and downstream societal vulnerability across this highly sensitive mountain system.

In this context, the present study employs high-resolution dynamical downscaling using the WRF model at 9 km spatial resolution, driven by bias-adjusted outputs from the MPI-ESM-HR CMIP6, to investigate projected changes in temperature, precipitation, and extreme precipitation across the Himalayan region under SSP2-4.5 and SSP5-8.5 scenarios. The study evaluates historical model performance against multiple observational and reanalysis datasets and examines regional (Western, Central, and Eastern Himalaya), seasonal, and elevation-dependent changes in mean climate and precipitation extremes. Particular emphasis is placed on understanding the spatial heterogeneity and elevation dependence of future hydroclimatic change, thereby demonstrating the added value of high-resolution dynamical downscaling for improving climate risk assessments across the Himalayan region.

## 2. Material and Methods

### 2.1. Study Area

The study focuses on the Indian Himalayan Region (IHR), extending approximately from 70°E to 95°E and 26°N to 37°N. The region is characterized by complex topography, large elevation gradients, and strong spatial variability in temperature and precipitation arising from the interaction of multiple atmospheric circulation systems.

To account for regional heterogeneity, the Himalayan domain is subdivided into three sectors: the Western Himalaya (WH), Central Himalaya (CH), and Eastern Himalaya (EH), as shown in Figure 1. These sub-regions represent distinct hydroclimatic regimes. The Western Himalaya is primarily influenced by extratropical western disturbances, particularly during winter, whereas the Eastern Himalaya is dominated by monsoonal precipitation driven by moisture transport from the Bay of Bengal. The Central Himalaya represents a transitional zone where both monsoonal and extratropical influences interact. This regional classification enables a more physically consistent interpretation of spatial variability in both mean climate and extremes.

### 2.2. Observational and Reanalysis Data

#### 2.2.1 APHRODITE Precipitation

Observed precipitation is obtained from the Asian Precipitation-Highly Resolved Observational Data Integration Towards Evaluation (APHRODITE) dataset (Yatagai et al., 2012), which provides a long-term, consistent, daily gridded precipitation dataset over Asia at

a spatial resolution of 0.25° × 0.25°. The dataset is constructed primarily from quality-controlled rain gauge observations collected from multiple national meteorological agencies and interpolated onto a regular grid using a modified Shepard distance-weighting scheme, with adjustments to better represent precipitation over complex terrain. Owing to its gauge-based formulation and specific development for hydrological applications, APHRODITE has been widely used in hydroclimatic studies across the Himalayan region, where accurately representing spatial precipitation variability is particularly challenging.

To develop a continuous precipitation record for the study period, two consistent versions of the dataset are used: APHRO_MA_025deg_V1101 for 1985–2007 and its extension release APHRO_MA_025deg_V1101_EXR1 for 2008–2014. These versions share the same underlying methodology but differ in temporal coverage and updates to the gauge observation network, and are concatenated to construct a continuous daily time series over the Indian Himalayan Region.

Compared to satellite-based precipitation product, Integrated Multi-satellitE Retrievals for GPM (IMERG) Version 07 Final Run dataset (Hou et al., 2014; Huffman et al., 2019), which are limited by relatively short temporal coverage and uncertainties in representing orographic precipitation processes over complex terrain. APHRODITE provides a longer and more consistent record suitable for climatological analysis (Bisht et al., 2021). Similarly, gauge-based gridded datasets such as India Meteorological Department (IMD) are constrained by sparse station coverage at higher elevations, which can introduce uncertainties in mountainous regions. Given these considerations, APHRODITE provides a robust dataset for evaluating the spatial distribution and seasonal variability of precipitation over the Himalayan region, while IMERG is used as a supplementary dataset to provide an independent satellite-based perspective on precipitation variability.

### 2.2.2 IMDAA reanalysis data

Temperature evaluation in this study is based on the Indian Monsoon Data Assimilation and Analysis (IMDAA) dataset, a high-resolution regional reanalysis covering the period 1979–2018 (Rani et al., 2021; Ashrit et al., 2020). The dataset is generated using the UK Met Office Unified Model and incorporates multiple observational sources, including surface measurements, atmospheric soundings, and satellite data, through a four-dimensional variational (4D-Var) data assimilation framework.

IMDAA provides atmospheric variables at approximately 12 km spatial resolution over the Indian region and offers improved representation of regional climate fields, particularly in areas with strong elevation gradients such as the Himalayan region. Owing to its high resolution and assimilation of diverse observational datasets, IMDAA is used as the primary reference dataset for evaluating near-surface air temperature.

Although the IMD provides gridded temperature datasets, these are available at a relatively coarse spatial resolution (~1° × 1°) (Srivastava et al., 2009), which limits their ability to resolve fine-scale variability associated with complex terrain. In addition, ERA5-Land temperature fields are examined to assess consistency in large-scale temperature patterns and to support comparison with WRF simulations.

As with other reanalysis products, IMDAA is influenced by model physics and data assimilation constraints, and uncertainties may persist in regions with sparse observational coverage, particularly at higher elevations. Nevertheless, it provides a physically consistent and high-resolution dataset suitable for evaluating temperature variability over the Himalayan region.

## 2.3. WRF Model configuration and experimental design

### 2.3.1. Bias-adjusted GCM forcing

Regional climate simulations were driven using a bias-adjusted CMIP6 atmospheric forcing dataset developed by Xu et al. (2021), which provides six-hourly large-scale atmospheric variables at a horizontal resolution of 1.25° × 1.25° for the historical period (1979–2014) and future SSP2-4.5 and SSP5-8.5 scenarios. The dataset includes key atmospheric variables required for regional climate modelling, including air temperature, geopotential height, wind components, relative humidity, and surface pressure. In this externally developed dataset, systematic biases in thermodynamic and dynamical fields are corrected using a Mean–Variance–Trend (MVT) adjustment approach, in which the climatological mean and variability are aligned with ERA5 reanalysis while preserving long-term climate change signals from CMIP6 simulations. High-frequency variability and synoptic-scale circulation patterns are retained to ensure dynamically consistent boundary conditions for regional downscaling over complex Himalayan terrain. MPI-ESM-HR was selected due to its relatively improved representation of South Asian monsoon circulation and the availability of high-temporal-resolution atmospheric fields required for regional dynamical downscaling.

### 2.3.2. WRF Model Configuration and Experiment

Dynamical downscaling is performed using the Advanced Research WRF (ARW) model version 4.5.2 (Skamarock et al., 2019). The model is configured with two nested domains to represent both large-scale atmospheric circulation and regional-scale processes. The outer domain (27 km resolution) covers South Asia, while the inner domain (9 km resolution) focuses on the Himalayan region, enabling improved representation of complex terrain and orographic precipitation processes. Both domains use 45 vertical levels extending up to 50 hPa.

Initial and lateral boundary conditions were provided using bias-adjusted six-hourly atmospheric fields derived from MPI-ESM-HR for the historical period (1979–2014) and future period (2031–2060) under SSP2-4.5 and SSP5-8.5 scenarios, and one-way nesting was employed.The physical parameterization schemes include the Morrison double-moment microphysics scheme, Yonsei University (YSU) planetary boundary layer scheme, Noah land surface model, RRTMG radiation schemes, MM5 surface layer scheme, and the Kain–Fritsch cumulus parameterization applied in the outer domain. A detailed summary of the model configuration and parameterization schemes is provided in Table 1.

## 2.4. Model Evaluation and Climate Indices

Climatological characteristics of temperature and precipitation are analysed using daily outputs from the WRF simulations and corresponding observational and reanalysis datasets. Seasonal climatologies are computed for annual, monsoon (June–September; JJAS), and winter (December–February; DJF) periods over the baseline period (1985–2014).

For model evaluation, WRF-simulated fields were interpolated to the native grids of the respective observational and reanalysis datasets (e.g., APHRODITE and IMDAA) using bilinear interpolation to ensure consistent spatial comparison. Model performance was evaluated using mean bias, root mean square error (RMSE), and spatial correlation (Table 2), where $X_{WRF}$ represents simulated values, Xref denotes reference observations/reanalysis data, n is the total number of grid points, and $\overline{X}$ indicates spatial mean values.

Projected changes in temperature and precipitation are computed relative to the historical baseline period (1985–2014). Temperature changes are expressed as absolute differences in equation (i) :

$$\Delta T = T_{\text{future}} - T_{Historical} \quad \ldots\ldots (i)$$

while precipitation changes are expressed as percentage anomalies as equation (ii):

$$\Delta P(\%) = \frac{P_{future} - P_{historical}}{P_{historical}} \times 100 \quad \ldots\ldots \text{(ii)}$$

Elevation-dependent characteristics are analysed by grouping model grid points into 500 m elevation bins based on model topography. The relationship between near-surface air temperature and elevation is quantified using linear regression to assess elevation-dependent warming across the Himalayan region.

Extreme precipitation characteristics are quantified using indices defined by the Expert Team on Climate Change Detection and Indices (ETCCDI), including annual maximum 1-day precipitation (Rx1day), maximum consecutive 5-day precipitation (Rx5day), frequency of extreme precipitation events (R95p), and the fractional contribution of extreme precipitation to total precipitation (R95pTOT). Rx1day represents the annual maximum of daily precipitation, while Rx5day denotes the maximum accumulated precipitation over any consecutive 5-day period within a year.

The R95p index is defined as the number of days in which daily precipitation exceeds the 95th percentile threshold of wet-day precipitation (≥1 mm day$^{-1}$). This percentile threshold is computed independently at each grid point using wet-day precipitation values from the historical baseline period (1985–2014), and is then held fixed and applied consistently to both historical and future simulations.

The fractional contribution of extreme precipitation (R95pTOT) is defined as equation (iii) :

$$R95pTOT = \frac{\sum P_{extreme}}{\sum P_{total}} \times 100 \quad \ldots\ldots \text{(iii)}$$

where Pextreme represents precipitation on days exceeding the grid-specific R95p threshold and Ptotal is the total precipitation accumulated over the same period.

Elevation-dependent changes in extreme precipitation are further analysed by computing these indices within each elevation band, enabling assessment of vertical variability in extreme event characteristics across the Himalayan region. All indices and calculations are performed consistently across historical and future simulations to ensure comparability of projected changes.

## 3. Results and Discussion

### 3.1. Evaluation of Historical Precipitation Climatology

The historical precipitation climatology simulated by WRF was primarily evaluated against the APHRODITE precipitation dataset for the period 1985–2014 due to its extensive spatial coverage across the Himalayan region. Additional comparisons with IMD gridded rainfall dataset, ERA5-Land, IMDAA, and GPM IMERG were performed using supplementary analyses (Figs. S1–S4) to assess the robustness of simulated precipitation patterns across datasets.

Figure 2 compares annual (Fig. 2a–c), monsoon (JJAS; Fig. 2d–f), and winter (DJF; Fig. 2g–i) precipitation climatology between WRF and the APHRODITE precipitation dataset. The APHRODITE dataset shows a pronounced precipitation gradient across the Himalayan region, with higher precipitation along the Himalayan foothills and comparatively lower precipitation over Ladakh and the adjoining Tibetan Plateau (Fig. 2a). WRF reproduces the overall annual spatial distribution reasonably well, with an annual mean bias of 0.23 mm $day^{-1}$, RMSE of 1.52 mm $day^{-1}$, and spatial correlation of 0.71 (Table 3). However, the annual bias pattern shows a broad wet bias along much of the Himalayan arc, with relatively stronger positive biases over the western Himalaya (Jammu & Kashmir, Himachal Pradesh, and Uttarakhand) and parts of the eastern Himalayan foothill region, while the adjoining plains south of the Himalaya exhibit pronounced dry biases (Fig. 2c).

During JJAS, which contributes the majority of annual precipitation across the region, WRF captures the overall monsoonal precipitation structure reasonably well, with the highest spatial correlation (0.78) and negligible mean bias (−0.06 mm $day^{-1}$), although the RMSE increases to 2.83 mm $day^{-1}$ due to strong spatial gradients in monsoonal precipitation (Table 3). Wet biases generally increase from the western to eastern Himalaya, consistent with stronger monsoonal influence in the eastern sector and strong orographic gradients in precipitation distribution (Bookhagen and Burbank, 2006; Palazzi et al., 2013). In contrast, the adjoining plains exhibit comparatively stronger dry biases during this season (Fig. 2f).

During winter (DJF), precipitation is primarily associated with Western Disturbances, and WRF shows a comparatively larger wet bias (0.37 mm $day^{-1}$), RMSE of 1.10 mm $day^{-1}$, and lower spatial correlation (0.65) (Table 3). The wet bias is strongest over the western Himalaya and gradually decreases eastward along the Himalayan arc, while the dry bias over the plains

is comparatively weaker than during annual and monsoon conditions (Fig. 2i). This likely reflects challenges in simulating winter precipitation over complex terrain, compounded by sparse high-elevation observations (Immerzeel et al., 2015).

Satellite products such as GPM IMERG may underestimate intense orographic precipitation over mountainous regions (Derin et al., 2016; Sun et al., 2018). Nevertheless, additional comparisons with supplementary datasets (Figs. S1–S4) show broadly consistent large-scale precipitation patterns, providing confidence in the WRF simulations for future climate projections.

### 3.2. Evaluation of Historical Temperature Climatology

The historical near-surface (2-m) air temperature simulated by WRF was primarily evaluated against the IMDAA regional reanalysis for the period 1985–2014 (Fig. 3), while additional comparisons with ERA5 were used to assess the robustness of simulated temperature patterns (Fig. S5).

Figure 3 compares annual (Fig. 3a–c), monsoon (JJAS; Fig. 3d–f), and winter (DJF; Fig. 3g–i) temperature climatology between WRF and IMDAA. Both datasets show a pronounced elevation-driven temperature gradient across the Himalayan region, with relatively warmer conditions over the foothills and adjoining plains and progressively cooler temperatures toward the higher Himalayan ranges and the Tibetan Plateau. WRF reproduces the annual spatial temperature distribution well, with a near-zero mean bias (0.12°C), RMSE of 2.65°C, and very high spatial correlation (0.98) (Table 4). However, the annual bias pattern reveals predominantly cold biases across large parts of the Himalayan arc, including sections of Jammu & Kashmir, Himachal Pradesh, Uttarakhand, Nepal, and parts of the eastern Himalaya, while localised warm biases are evident over parts of Ladakh (Fig. 3c). Similar large-scale temperature gradients and bias characteristics are also evident in the comparison with ERA5 (Fig. S5).

During JJAS, WRF captures the large-scale monsoon-season temperature structure with a high spatial correlation (0.98) but exhibits a moderate cold bias (−0.66°C) and RMSE of 2.92°C (Table 4). The bias pattern indicates stronger cold anomalies across the higher Himalayan ranges and Tibetan Plateau, while relatively warmer conditions persist over the adjoining plains (Fig. 3f). These differences likely reflect uncertainties in cloud cover, land–atmosphere interactions, and surface moisture processes associated with the South Asian summer monsoon.

During winter (DJF), both datasets show markedly colder temperatures over the higher Himalayan ranges and Tibetan Plateau. WRF maintains a high spatial correlation (0.98) but shows a moderate warm bias (0.88°C) and RMSE of 3.03°C (Table 4). The bias pattern remains spatially heterogeneous, with cold biases over several high-elevation regions and localised warm anomalies across parts of Ladakh and adjoining areas (Fig. 3i), likely reflecting uncertainties related to snow–albedo feedbacks, surface energy balance, and boundary-layer processes (Dimri et al., 2018). The strong agreement with IMDAA and the consistency with ERA5 provide confidence in using the WRF simulations to analyse elevation-dependent temperature behaviour and to project future climate.

### 3.3. Elevation-dependent temperature gradients across the Himalayan regions

Figure 4 illustrates the elevation–temperature relationship across the Western Himalaya (WH), Central Himalaya (CH), and Eastern Himalaya (EH) during the historical period (1985–2014), derived using elevation-bin averages from IMDAA and WRF simulations. Across all regions, mean near-surface air temperature decreases systematically with increasing elevation, highlighting the dominant role of topography in controlling thermal gradients across the Himalayan region.

WRF reproduces the observed elevation–temperature relationship reasonably well across most elevation ranges (Fig. 4a–i). In the annual climatology (Fig. 4a–c), the Western and Central Himalaya exhibit relatively steeper temperature gradients at higher elevations, while the Eastern Himalaya remains comparatively warmer at similar elevations, likely reflecting stronger monsoonal influence and lower continentality in the eastern sector. Small divergences between WRF and IMDAA become more evident above ~4000–5000 m, particularly in the Western and Central Himalaya.

During JJAS (Fig. 4d–f), temperature gradients become comparatively weaker across all three regions due to enhanced cloud cover, increased atmospheric moisture, and reduced diurnal temperature variability associated with the South Asian summer monsoon. In the Western and Central Himalaya, WRF shows strong agreement with IMDAA up to approximately 2000–3000 m, beyond which the model tends to simulate comparatively cooler temperatures at higher elevations. The Eastern Himalaya exhibits relatively better agreement across most elevation ranges, with only minor divergence at the highest elevations.

During DJF (Fig. 4g–i), the temperature decrease with elevation becomes more pronounced, particularly in the Western and Central Himalaya, reflecting stronger radiative cooling, snow cover influence, and stable winter atmospheric conditions. WRF shows strong agreement with IMDAA across most elevation ranges in all three Himalayan regions, with only minor divergence at elevations above ~5000 m, particularly in the Central Himalaya. These results indicate that the model effectively captures elevation-dependent temperature gradients and seasonal variability across the Himalayan arc.

### 3.4. Projected Temperature Change in the Himalaya

Future temperature changes across the Himalayan region were analysed using high-resolution WRF simulations dynamically downscaled from bias-corrected MPI-ESM-HR projections under SSP2-4.5 and SSP5-8.5 scenarios. Figures 5a and 5b show projected warming during the mid-21st century period (2031–2060) relative to the historical baseline (1985–2014). Both scenarios indicate widespread warming across the Himalayan region, although the magnitude of warming differs substantially between scenarios.

Under SSP2-4.5, projected warming is generally around 1–2°C across much of the Himalayan arc (Fig. 5a). Under SSP5-8.5, warming intensifies to approximately 2–4°C, with stronger warming over higher elevations, particularly across the northern Himalayan region and the Tibetan Plateau (Fig. 5b). The additional warming under SSP5-8.5 relative to SSP2-4.5 ranges from approximately 0.5–2°C across much of the domain (Fig. 5c), highlighting the strong sensitivity of regional temperature change to future emission pathways.

Regional temperature anomaly time series further highlight differences across the Western Himalaya (WH), Central Himalaya (CH), and Eastern Himalaya (EH) (Fig. 5d–f). All three regions show persistent warming under both scenarios, with divergence between SSP2-4.5 and SSP5-8.5 becoming more pronounced after the early 2040s. The Central Himalaya exhibits the strongest warming, followed by the Western Himalaya, while the Eastern Himalaya shows comparatively lower warming. By the late 2050s, regional warming under SSP5-8.5 approaches approximately 3°C in the Western and Central Himalaya and around 2.5°C in the Eastern Himalaya, whereas SSP2-4.5 warming remains comparatively lower across all regions.

These results indicate substantial warming across the Himalayan region during the mid-21st century, with amplified warming at higher elevations and significantly stronger temperature increases under the high-emission scenario

### 3.5. Spatial and Temporal Evolution of Projected Mean Precipitation

Future precipitation changes across the Himalayan region were analysed under SSP2-4.5 and SSP5-8.5 scenarios relative to the historical baseline period (1985–2014). Figure 6A shows projected percentage changes in annual, monsoon (JJAS), and winter (DJF) precipitation for the near-future (2031–2045) and late-future (2046–2060) periods, while Figure 6B presents regional precipitation anomalies for the Western Himalaya (WH), Central Himalaya (CH), and Eastern Himalaya (EH).

Annual precipitation projections indicate a non-monotonic response across the Himalayan region. During the near-future period, precipitation increases are more widespread under both scenarios, particularly under SSP5-8.5, with positive anomalies of approximately 10–40% across parts of the western Himalaya, Karakoram, and sections of the central Himalayan arc (Fig. 6A; a,c). In the late-future period, annual precipitation changes become more spatially heterogeneous, with localized increases of approximately 0–20% persisting over parts of Jammu & Kashmir and Ladakh, while sections of Himachal Pradesh, Uttarakhand, and the adjoining Indo-Gangetic plains exhibit drying of approximately −10 to −20% under both scenarios (Fig. 6A; b,d). This non-monotonic precipitation response is consistent with earlier studies highlighting substantial spatial variability in future Himalayan precipitation projections under changing climate conditions (Chen and Frauenfeld, 2014; Sanjay et al., 2017).

During the monsoon season (JJAS), which contributes the majority of annual precipitation across the Himalayan region, both scenarios project increased precipitation during the near-future period, with stronger increases under SSP5-8.5 where anomalies of approximately 20–50% occur across parts of the western Himalaya, Himalayan foothills, and sections of the central Himalayan region (Fig. 6A; e,g). These increases are consistent with the enhanced atmospheric moisture availability expected under warmer conditions and the associated intensification of monsoonal precipitation (Held and Soden, 2006; Kitoh et al., 2013). In the late-future period, monsoon precipitation changes become more spatially heterogeneous, with reductions of approximately −10 to −30% across parts of Himachal Pradesh, Uttarakhand, the Central Himalaya, and the Eastern Himalaya, while localized increases persist over the northwestern Himalayan–Karakoram sector (Fig. 6A; f,h). This spatial redistribution suggests that regional circulation changes may modulate thermodynamically driven increases in monsoon precipitation under future warming (Krishnan et al., 2013).

Winter precipitation exhibits a contrasting response. Under SSP2-4.5, DJF precipitation increases by approximately 10–40% across much of the Himalayan arc and adjoining plains during the near-future period (Fig. 6A;i). In the late-future period, these positive anomalies weaken but remain generally positive (0–20%) across much of the Himalayan region, while the plains show a more mixed response (Fig. 6A; j). Under SSP5-8.5, the near-future period shows localized drying of approximately −10 to −30%, particularly across Uttarakhand and parts of the Central Himalaya, while other regions exhibit mixed positive and negative anomalies (Fig. 6A;k). By the late-future period, the intensity of drying weakens in some locations but expands spatially across Uttarakhand, Himachal Pradesh, and Jammu & Kashmir, with broader negative anomalies of approximately 0 to −30% across parts of the Himalayan arc. In contrast, much of the adjoining plains also experiences drying, except for localized increases of up to 20–40% over parts of Assam and Meghalaya (Fig. 6A;l) highlighting uncertainties in future winter precipitation responses reported in earlier studies (Hunt et al., 2018; Krishnan et al., 2019).

Regional precipitation anomalies further highlight contrasting temporal responses across the three Himalayan sub-regions (Fig. 6B). The Western Himalaya (WH) shows a pronounced increase during the early projection period, with anomalies peaking at approximately 25–30% before declining toward near-normal conditions by the late 2050s. The Central Himalaya (CH) exhibits stronger fluctuations, with anomalies reaching nearly 20–30% followed by a shift toward negative anomalies during the late-future period. In contrast, the Eastern Himalaya (EH) shows comparatively smaller increases of approximately 5–10% during the near-future period, followed by declines of nearly 5–10% toward the late-future period. These regional trajectories further highlight the non-monotonic nature of future precipitation changes across the Himalayan region.

### 3.6. Elevation-Dependent Precipitation Change

Changes in precipitation across the Himalayan region are strongly influenced by elevation-dependent processes associated with orographic uplift, monsoonal moisture transport, and regional circulation variability. Examining precipitation responses across different elevation zones is therefore important for understanding future hydroclimatic changes in snow-dominated headwater regions and mid-elevation catchments that are highly sensitive to changes in seasonal precipitation regimes. Figure 7 illustrates elevation-dependent changes in mean precipitation ($\Delta P$; mm day$^{-1}$) during 2031–2060 relative to the historical baseline period (1985–

2014) across the Western Himalaya (WH), Central Himalaya (CH), and Eastern Himalaya (EH), using 500 m elevation bins.

Annual precipitation changes remain relatively modest across all regions, generally within ±0.5 mm day$^{-1}$ (Fig. 7a–c). The Western Himalaya shows weak positive changes across most elevations, while the Central and Eastern Himalaya exhibit stronger increases at mid-elevations (~1500–3000 m), with peak anomalies of approximately 0.5–0.6 mm day$^{-1}$. Negative changes are primarily confined to lower elevations in parts of the Central and Eastern Himalaya.

The strongest elevation-dependent response occurs during JJAS (Fig. 7d–f). In the Western Himalaya, SSP5-8.5 projects stronger mid-elevation increases of nearly 1 mm day$^{-1}$ between ~1000–2500 m compared with SSP2-4.5. The Central Himalaya shows the largest monsoon intensification, with peak increases of approximately 1–1.5 mm day$^{-1}$ around 1500–2500 m under both scenarios. In the Eastern Himalaya, SSP2-4.5 projects comparatively stronger increases, while SSP5-8.5 shows reduced precipitation at lower elevations. The stronger response at mid-elevations likely reflects enhanced orographic uplift and moisture convergence along the windward Himalayan slopes, where monsoonal precipitation is climatologically concentrated (Bookhagen and Burbank, 2006; Sanjay et al., 2017).

Winter (DJF) precipitation changes are comparatively weaker and more variable (Fig. 7g–i). In the Western Himalaya, SSP2-4.5 shows positive changes of up to 0.7–0.8 mm day$^{-1}$, whereas SSP5-8.5 projects weak negative anomalies across most elevations. The Central Himalaya shows modest positive changes under both scenarios, while the Eastern Himalaya exhibits negative changes under SSP5-8.5 at lower to mid elevations. These changes are particularly important because winter precipitation contributes substantially to seasonal snow accumulation and glacier mass balance in high-elevation catchments (Immerzeel et al., 2020; Huss and Hock, 2018).

### 3.7. Projected Changes in Extreme Precipitation Intensity

Extreme precipitation is expected to intensify under continued atmospheric warming due to increased moisture-holding capacity and enhanced precipitation efficiency during intense rainfall events. Over the Himalayan region, such changes are particularly important because short-duration and multi-day extreme precipitation events are closely associated with flash floods, landslides, debris flows, and other hydrogeomorphic hazards. Figure 8 presents projected changes in annual maximum 1-day precipitation (Rx1day; mm day$^{-1}$) and maximum

consecutive 5-day precipitation (Rx5day; mm) during 2031–2060 relative to the historical baseline period (1985–2014) under SSP2-4.5 and SSP5-8.5 scenarios.

Under SSP2-4.5, both Rx1day and Rx5day show increases of approximately 5–15 mm across much of the western Himalaya, including Ladakh, Jammu & Kashmir, and western Himachal Pradesh, along with parts of the Central and Eastern Himalaya (Fig. 8a,c), indicating enhanced short-duration and multi-day precipitation extremes. In contrast, eastern Himachal Pradesh and western and eastern Uttarakhand exhibit localized declines of approximately −5 to −10 mm, along with additional negative anomalies across parts of the adjoining Indo-Gangetic plains.

Under SSP5-8.5, extreme precipitation intensification becomes stronger but spatially heterogeneous (Fig. 8b,d). Both Rx1day and Rx5day increase by approximately 5–15 mm, with localized increases exceeding 15 mm, across the western Himalaya (Jammu & Kashmir, Himachal Pradesh, and parts of Ladakh) and the eastern Himalayan region. In contrast, parts of Uttarakhand and the adjoining plains of Uttar Pradesh exhibit declines of approximately −5 to −15 mm. The stronger increases in Rx5day suggest greater intensification of prolonged extreme precipitation events under the high-emission scenario.

The projected intensification of both short-duration and multi-day precipitation extremes has important implications for flash floods, landslides, and debris-flow hazards across the Himalayan region (Bookhagen and Burbank, 2010; Allen et al., 2016; Wester et al., 2019). The stronger response under SSP5-8.5 further highlights the sensitivity of extreme precipitation to higher greenhouse gas forcing (Seneviratne et al., 2021).

### 3.8. Projected Changes in Frequency and Fractional Contribution of Extreme Precipitation

In addition to changes in extreme precipitation intensity, future hydroclimatic risk is also strongly influenced by changes in the frequency of extreme events and their contribution to total annual precipitation. An increase in the occurrence of extreme precipitation events implies greater recurrence of flood-generating rainfall, while an increasing fractional contribution of extremes indicates a transition toward a more episodic and extreme-dominated precipitation regime. Figure 9 presents projected changes in the frequency of extreme precipitation events (R95p; days $yr^{-1}$) and their contribution to total annual precipitation (%) during 2031–2060 relative to the historical baseline period (1985–2014). Extreme events are defined using the

historical 95th percentile threshold for wet-day precipitation, following the standard ETCCDI definitions (Zhang et al., 2011; Sillmann et al., 2013a).

Under SSP2-4.5, the frequency of extreme precipitation events increases by approximately 2–4 days $yr^{-1}$ across much of the Himalayan arc, particularly over the western and central Himalaya (Fig. 9a), while parts of the adjoining Indo-Gangetic plains show reductions of approximately −2 to −4 days $yr^{-1}$. Under SSP5-8.5, increases become stronger and more spatially extensive over the western Himalaya, reaching nearly 4–6 additional days $yr^{-1}$, while parts of the central and eastern Himalaya exhibit a more heterogeneous response with localized negative anomalies (Fig. 9b).

The contribution of extreme precipitation to annual rainfall also increases across much of the Himalayan region (Fig. 9c,d). Under SSP2-4.5, extreme events contribute approximately 2–6% more to annual precipitation across large parts of the Himalayan arc, while portions of the adjoining plains show declines of approximately −5 to −10% (Fig. 9c). Under SSP5-8.5, the contribution of extremes increases further by approximately 5–10%, particularly across the western Himalaya, although localized negative anomalies persist across parts of the plains and eastern sector (Fig. 9d).

Together with the projected increases in Rx1day and Rx5day (Fig. 8), these results indicate that future precipitation across the Himalaya is likely to become not only more intense, but also more frequent and increasingly concentrated in extreme rainfall events. This has important implications for flood risk, erosion, and downstream water availability across the region (Immerzeel et al., 2020; Lutz et al., 2014; Huss and Hock, 2018).

### 3.9. Elevation-Dependent Changes in Extreme Precipitation

The response of extreme precipitation to climate change is strongly influenced by elevation-dependent thermodynamic and orographic processes across mountainous regions. Changes in extreme precipitation with elevation are particularly important across the Himalaya because different elevation zones exhibit distinct precipitation regimes, snow–rain transitions, moisture transport characteristics, and hydrogeomorphic sensitivities. Understanding how precipitation extremes vary across elevation bands is therefore critical for assessing future risks associated with flash floods, landslides, debris flows, and cryospheric hazards in Himalayan catchments. Figure 10 illustrates the elevation-dependent changes in extreme precipitation characteristics across the Western Himalaya (WH), Central Himalaya (CH), and Eastern Himalaya (EH)

during 2031–2060 relative to the historical baseline period (1985–2014) under SSP2-4.5 and SSP5-8.5 scenarios.

The frequency of extreme precipitation events generally increases across most elevation bands in all three sub-regions (Fig. 10a–c). In the Western Himalaya, both scenarios show consistent increases of approximately 2–4 days $yr^{-1}$, with the strongest increases occurring at lower to mid elevations (~500–2000 m). The Central Himalaya exhibits greater variability, with near-zero to slightly negative changes at lower elevations under SSP5-8.5, followed by increases of approximately 2–4 days $yr^{-1}$ at mid elevations. The Eastern Himalaya shows comparatively moderate but persistent increases of approximately 1–3 days $yr^{-1}$ across most elevations.

The contribution of extreme precipitation to total rainfall also increases across most elevation zones (Fig. 10d–f). In the Western Himalaya, the contribution of extremes increases by approximately 1–4% under SSP2-4.5 and nearly 4–6% under SSP5-8.5. The Central Himalaya shows more variable but generally positive changes of approximately 1–5%, while the Eastern Himalaya exhibits relatively consistent increases of approximately 2–5%, particularly at lower to mid elevations.

These results indicate that future precipitation across the Himalayan region is projected to become increasingly concentrated in extreme events across multiple elevation zones. Such changes may enhance flood hazards, rain-on-snow events, and downstream hydrological risks in high-elevation catchments (Pomeroy et al., 2012; Carrivick and Tweed, 2016; Rounce et al., 2023).

## 4. Summary and Conclusions

This study presents a high-resolution assessment of projected changes in temperature, mean precipitation, and extreme precipitation across the Himalayan region using dynamical downscaling with the WRF model at 9 km resolution, driven by bias-adjusted MPI-ESM-HR CMIP6 model under SSP2–4.5 and SSP5–8.5. Model evaluation against multiple observational and reanalysis datasets demonstrates that the WRF simulations realistically reproduce the large-scale spatial distribution, seasonal variability, and elevation-dependent characteristics of temperature and precipitation across the Himalayan region. In particular, the model captures the observed temperature–elevation relationship and major regional hydroclimatic contrasts across the Western, Central, and Eastern Himalaya, providing confidence in the reliability of the future climate projections.

The projected future climate over the Himalaya indicates widespread warming under both emission scenarios during 2031–2060, with substantially stronger warming under SSP5-8.5. Temperature increases are generally around 1–2°C under SSP2-4.5 and 2–4°C under SSP5-8.5, with amplified warming over higher elevations and the northern Himalayan ranges, indicating the continued importance of elevation-dependent warming processes across the region. Regional differences are also evident, with comparatively stronger warming over parts of the Western and Central Himalaya relative to the Eastern Himalaya. Such warming is likely to have important implications for glacier mass balance, snow cover persistence, meltwater availability, and downstream hydrological regimes across Himalayan river basins.

Projected precipitation changes exhibit substantially greater spatial and temporal heterogeneity compared to temperature. Annual and monsoonal precipitation generally increase during the near-future period, particularly across parts of the Western and Central Himalaya, with localized precipitation increases of approximately 10–40%, especially under SSP5-8.5. However, precipitation responses become increasingly heterogeneous during the late-future period, with localized drying of 10–20% emerging across parts of Himachal Pradesh, Uttarakhand, and adjoining Indo-Gangetic plains. Elevation-dependent analyses further indicate that precipitation responses vary considerably across elevation zones and Himalayan sub-regions. During the monsoon season, mid-elevation zones (~1500–3000 m) generally exhibit comparatively stronger positive precipitation anomalies, consistent with enhanced moisture transport and orographic uplift along the Himalayan slopes. In contrast, higher elevations show more spatially variable responses, especially across the Central and Eastern Himalaya, whereas the Western Himalaya exhibits relatively more coherent precipitation increases. Winter precipitation responses remain regionally contrasting, with increases under SSP2-4.5 but localized reductions under SSP5-8.5, suggesting potential implications for seasonal snow accumulation and glacier recharge processes across high-elevation catchments.

The simulations further indicate a substantial intensification of extreme precipitation characteristics across much of the Himalayan region. Both Rx1day and Rx5day show increases of approximately 5–15 mm under future warming, with localized increases exceeding 15 mm under SSP5-8.5, particularly across the Western Himalaya and parts of the Eastern Himalaya. In addition to increased intensity, the frequency of extreme precipitation events also increases by approximately 2–6 days $yr^{-1}$ across many parts of the Himalayan arc, while the contribution of extreme events to annual precipitation increases by nearly 2–10%. Elevation-dependent

599 analyses further show that the strongest increases in extreme-event frequency and contribution
600 generally occur across lower to mid-elevation zones, particularly in the Western Himalaya.
601 These findings collectively suggest a transition toward a more extreme-dominated
602 hydroclimatic regime, in which changes in precipitation variability and extremes become more
603 pronounced than changes in mean precipitation. Such changes are likely to increase the risks
604 of flash floods, landslides, debris flows, rain-on-snow events, and glacial lake outburst floods
605 across environmentally fragile Himalayan catchments.

606 Although the present study is based on a single driving global climate model and one WRF
607 configuration, the high-resolution dynamically downscaled simulations substantially improve
608 the representation of complex Himalayan topography, regional hydroclimatic gradients, and
609 elevation-dependent climate responses compared to coarse-resolution GCM outputs. The
610 results highlight the importance of high-resolution regional climate modelling for resolving
611 fine-scale hydroclimatic variability across the Himalaya and provide improved insight into
612 future changes in temperature, precipitation, and extreme precipitation characteristics across
613 the Western, Central, and Eastern Himalaya. These projections can support future hydrological,
614 cryospheric, hazard, and water-resource assessments across the region. Future work should
615 incorporate multi-model ensembles, convection-permitting simulations, and coupled
616 hydroclimatic analyses to further reduce projection uncertainties and improve understanding
617 of regional climate-change impacts across the Himalayan region.

**Acknowledgements:**

The authors acknowledge the computational support provided by the PARAM Porul HPC facility at the National Institute of Technology Tiruchirappalli and the PARAM Ganga HPC facility at IIT Roorkee under the National Supercomputing Mission (NSM), Government of India. Financial support from the National Remote Sensing Centre (NRSC), Indian Space Research Organisation (ISRO), Government of India, through the sponsored R&D project is also gratefully acknowledged. The authors further acknowledge the use of AI-assisted tools for improving the language and readability of the manuscript.

**Declarations:**

**Funding:** This research was supported by the National Remote Sensing Centre (NRSC), Indian Space Research Organisation (ISRO), Department of Space, Government of India, through the sponsored R&D project

**Conflicts of interest:** The authors declare no conflict of interest.

**Author contributions:** Kuldeep Sharma led the conceptualization of the study, model setup, methodological development, analysis, preparation of the original draft, and overall coordination of the work. Vishal Singh contributed to the analysis as well as manuscript editing and revision. Deepak Singh Bisht contributed to the analysis and methodological framework. Somesh Kumar was responsible for data acquisition, including reanalysis and observational datasets. Sahidul Islam provided technical guidance related to model setup and contributed to manuscript revision. Mohammad Sajeed and Ramesh Bulusu supported the technical setup of the WRF model and its performance optimization.

**Data availability:** The datasets used in this study are available from the corresponding author upon reasonable request.

**Ethics approval:** Not applicable.

**Consent to participate:** Not applicable.

**Consent for publication:** All authors have approved the manuscript for publication.

645

**References:**


Allen MR, Ingram WJ (2002) Constraints on future changes in climate and the hydrologic cycle. Nature 419:224–232. https://doi.org/10.1038/nature01092

Allen SK, Zhang G, Wang W, et al (2019) Potentially dangerous glacial lakes across the Tibetan Plateau revealed using a large-scale automated assessment approach. Sci Bull (Beijing) 64:435–445. https://doi.org/10.1016/j.scib.2019.03.011

Ashrit R, Indira Rani S, Kumar S, others (2020) IMDAA regional reanalysis: performance evaluation during Indian summer monsoon season. Journal of Geophysical Research: Atmospheres 125:e2019JD030973. https://doi.org/10.1029/2019JD030973

Bisht DS, Chowdhury B, Rawat SS, others (2024) Performance ranking of global precipitation estimates over data scarce Western Himalayan Region of India. Theor Appl Climatol 155:7515–7537. https://doi.org/10.1007/s00704-024-05069-4

Bookhagen B, Burbank DW (2010) Toward a complete Himalayan hydrological budget: spatiotemporal distribution of snowmelt and rainfall and their impact on river discharge. J Geophys Res 115:F03019. https://doi.org/10.1029/2009JF001426

Bookhagen B, Burbank DW (2006) Topography, relief, and TRMM-derived rainfall variations along the Himalaya. Geophys Res Lett 33:L08405. https://doi.org/10.1029/2006GL026037

Boos WR, Kuang Z (2010) Dominant control of the South Asian monsoon by orographic insulation versus plateau heating. Nature 463:218–222. https://doi.org/10.1038/nature08707

Cannon F, Carvalho LM v, Jones C, Bookhagen B (2015) Multi-annual variations in winter westerly disturbance activity affecting the Himalaya. Clim Dyn 44:441–455. https://doi.org/10.1007/s00382-014-2248-8

Carrivick JL, Tweed FS (2016) A global assessment of the societal impacts of glacial lake outburst floods. Glob Planet Change 144:1–16. https://doi.org/10.1016/j.gloplacha.2016.07.001

Chen F, Dudhia J (2001) Coupling an advanced land surface–hydrology model with the Penn State–NCAR MM5 modeling system. Part I: model implementation and sensitivity. Mon Weather Rev 129:569–585. https://doi.org/10.1175/1520-0493(2001)129<0569:CAALSH>2.0.CO;2

Chen L, Frauenfeld OW (2014) A comprehensive evaluation of precipitation simulations over the Tibetan Plateau. Journal of Geophysical Research: Atmospheres 119:. https://doi.org/10.1002/2013JD021190

Chou C, Neelin JD, Chen CA, Tu JY (2013) Evaluating the rich-get-richer mechanism in tropical precipitation change under global warming. J Clim 26:5687–5704. https://doi.org/10.1175/JCLI-D-12-00323.1

Derin Y, Anagnostou EN, Anagnostou MN, others (2016) Evaluation of GPM-era satellite precipitation products over complex terrain. J Hydrometeorol 17:1817–1835. https://doi.org/10.1175/JHM-D-15-0197.1

Dimri AP, Kumar D, Choudhary A, Maharana P (2018) Future changes over the Himalayas: Maximum and minimum temperature. Glob Planet Change 162:212–234. https://doi.org/10.1016/j.gloplacha.2018.01.015

Dimri AP, Niyogi D, Barros AP, others (2015) Western disturbances: a review. Reviews of Geophysics 53:225–246. https://doi.org/10.1002/2014RG000460

Dube A, Ashrit R, Ashish A, others (2014) Forecasting the heavy rainfall during Himalayan flooding—June 2013. Weather Clim Extrem 4:22–34. https://doi.org/10.1016/j.wace.2014.03.004

Fischer EM, Knutti R (2016) Observed heavy precipitation increase confirms theory and early models. Nat Clim Chang 6:986–991. https://doi.org/10.1038/nclimate3110

Giorgi F, Gutowski WJ (2015) Regional dynamical downscaling and the CORDEX initiative. Annu Rev Environ Resour 40:467–490. https://doi.org/10.1146/annurev-environ-102014-021217

Goswami BN, Venugopal V, Sengupta D, others (2006) Increasing trend of extreme rain events over India in a warming environment. Science (1979) 314:1442–1445. https://doi.org/10.1126/science.1132027

Held IM, Soden BJ (2006) Robust responses of the hydrological cycle to global warming. J Clim 19:5686–5699. https://doi.org/10.1175/JCLI3990.1

Hong SY, Noh Y, Dudhia J (2006) A new vertical diffusion package with an explicit treatment of entrainment processes. Mon Weather Rev 134:2318–2341. https://doi.org/10.1175/MWR3199.1

Hou AY, Kakar RK, Neeck S, others (2014) The Global Precipitation Measurement mission. Bull Am Meteorol Soc 95:701–722. https://doi.org/10.1175/BAMS-D-13-00164.1

Huffman GJ, Bolvin DT, Nelkin EJ, Tan J (2019) Integrated Multi-Satellite Retrievals for GPM (IMERG) technical documentation

Hunt KMR, Turner AG, Shaffrey LC (2018) The evolution, seasonality, and impacts of western disturbances. Quarterly Journal of the Royal Meteorological Society 144:278–290. https://doi.org/10.1002/qj.3200

Huss M, Hock R (2018) Global-scale hydrological response to future glacier mass loss. Nat Clim Chang 8:135–140. https://doi.org/10.1038/s41558-017-0049-x

Iacono MJ, Delamere JS, Mlawer EJ, others (2008) Radiative forcing by long-lived greenhouse gases: calculations with the AER radiative transfer models. J Geophys Res 113:D13103. https://doi.org/10.1029/2008JD009944

Immerzeel WW, Lutz AF, Andrade M, others (2020) Importance and vulnerability of the world's water towers. Nature 577:364–369. https://doi.org/10.1038/s41586-019-1822-y

Immerzeel WW, van Beek LPH, Bierkens MFP (2010) Climate change will affect the Asian water towers. Science (1979) 328:1382–1385. https://doi.org/10.1126/science.1183188

721 Kain JS (2004) The Kain–Fritsch convective parameterization: an update. Journal of Applied
722 Meteorology 43:170–181. https://doi.org/10.1175/1520-
723 0450(2004)043<0170:TKCPAU>2.0.CO;2

724 Kraaijenbrink P, Bierkens M, Lutz A, others (2017) Impact of a global temperature rise of 1.5
725 degrees Celsius on Asia's glaciers. Nature 549:257–260. https://doi.org/10.1038/nature23878

726 Krishnan R, others (2019) Unravelling climate change in the Hindu Kush Himalaya: Rapid
727 warming in the mountains and increasing extremes. In: The Hindu Kush Himalaya Assessment.
728 Springer, Cham, pp 57–97

729 Krishnan R, Sabin TP, Ayantika DC, others (2013) Will the South Asian monsoon overturning
730 circulation stabilize any further? Clim Dyn 40:187–211. https://doi.org/10.1007/s00382-012-
731 1317-0

732 Lee J-Y, Marotzke J, Bala G, others (2021) Future global climate: Scenario-based projections
733 and near-term information. In: Climate Change 2021: The Physical Science Basis. Cambridge
734 University Press, pp 553–672

735 Lutz AF, Immerzeel WW, Shrestha AB, Bierkens MFP (2014) Consistent increase in High
736 Asia's runoff due to increasing glacier melt and precipitation. Nat Clim Chang 4:587–592.
737 https://doi.org/10.1038/nclimate2237

738 Morrison H, Thompson G, Tatarskii V (2009) Impact of cloud microphysics on the
739 development of trailing stratiform precipitation in a simulated squall line: comparison of one-
740 and two-moment schemes. Mon Weather Rev 137:991–1007.
741 https://doi.org/10.1175/2008MWR2556.1

742 Muñoz-Sabater J, Dutra E, Agustí-Panareda A, others (2021) ERA5-Land: A state-of-the-art
743 global reanalysis dataset for land applications. Earth Syst Sci Data 13:4349–4383.
744 https://doi.org/10.5194/essd-13-4349-2021

745 O'Gorman PA (2015) Precipitation extremes under climate change. Curr Clim Change Rep
746 1:49–59. https://doi.org/10.1007/s40641-015-0009-3

747 Palazzi E, Filippi L, von Hardenberg J (2017) Insights into elevation-dependent warming in
748 the Himalayas from CMIP5 models. Clim Dyn 48:3991–4008. https://doi.org/10.1007/s00382-
749 016-3316-z

750 Palazzi E, Mortarini L, Terzago S, von Hardenberg J (2019) Elevation-dependent warming in
751 global climate model simulations at high spatial resolution. Clim Dyn 52:2685–2702.
752 https://doi.org/10.1007/s00382-018-4287-z

753 Palazzi E, von Hardenberg J, Provenzale A (2013) Precipitation in the Hindu Kush–
754 Karakoram–Himalaya: observations and future scenarios. Journal of Geophysical Research:
755 Atmospheres 118:85–100. https://doi.org/10.1029/2012JD018697

756 Pant M, Bhatla R, Ghosh S, et al. (2024) How climate change is affecting the summer monsoon
757 extreme rainfall pattern over the Indo-Gangetic Plains of India: present and future perspectives.
758 Clim Dyn 62:1055–1075. https://doi.org/10.1007/s00382-023-06953-x

759 Paulson CA (1970) The mathematical representation of wind speed and temperature profiles
760 in the unstable atmospheric surface layer. Journal of Applied Meteorology 9:857–861.
761 https://doi.org/10.1175/1520-0450(1970)009<0857:TMROWS>2.0.CO;2

762 Pattnayak KC, Awasthi A, Sharma K, Pattnayak BB (2023) Fate of rainfall over the North
763 Indian states in the 1.5 and 2 °C warming scenarios. Earth Space Sci 10:e2022EA002671.
764 https://doi.org/10.1029/2022EA002671

765 Pepin N, Bradley RS, Diaz HF, others (2015) Elevation-dependent warming in mountain
766 regions of the world. Nat Clim Chang 5:424–430. https://doi.org/10.1038/nclimate2563

767 Pomeroy JW, Fang X, Ellis C (2012) Sensitivity of snowmelt hydrology in Marmot Creek,
768 Alberta, to forest cover disturbance. Hydrol Process 26:1892–1905.
769 https://doi.org/10.1002/hyp.9248

770 Prein AF, others (2015) A review on regional convection-permitting climate modeling:
771 Demonstrations, prospects, and challenges. Reviews of Geophysics 53:323–361.
772 https://doi.org/10.1002/2014RG000475

773 Pritchard DMW, Forsythe N, Fowler HJ, et al (2019) Evaluation of Upper Indus near-surface
774 climate representation by WRF in the High Asia Refined Analysis. J Hydrometeorol 20:467–
775 487. https://doi.org/10.1175/JHM-D-18-0030.1

776 Rani SI, Arulalan T, George JP, others (2021) IMDAA: high-resolution satellite-era reanalysis
777 for the Indian monsoon region. J Clim 34:5109–5133. https://doi.org/10.1175/JCLI-D-20-
778 0412.1

779 Rounce DR, Hock R, Shean DE, others (2023) Global glacier change in the 21st century: Every
780 increase in temperature matters. Science (1979) 379:78–83.
781 https://doi.org/10.1126/science.abo1324

782 Roxy MK, Ghosh S, Pathak A, others (2017) A threefold rise in widespread extreme rain events
783 over central India. Nat Commun 8:708. https://doi.org/10.1038/s41467-017-00744-9

784 Sabin TP, Krishnan R, Vellore RK, others (2020) Climate change over the Himalayas. In:
785 Krishnan R, Sanjay J, Gnanaseelan C, others (eds) Assessment of Climate Change over the
786 Indian Region. Springer, Singapore, pp 207–222

787 Sanjay J, Krishnan R, Shrestha AB, others (2017) Downscaled climate change projections for
788 the Hindu Kush Himalaya region using CORDEX South Asia regional climate models.
789 Advances in Climate Change Research 8:185–198. https://doi.org/10.1016/j.accre.2017.08.003

790 Seneviratne SI, others (2021) Weather and climate extreme events in a changing climate. In:
791 Climate Change 2021: The Physical Science Basis. Cambridge University Press

792 Sharma K, Ashrit R, Kumar S, others (2021) Unified model rainfall forecasts over India during
793 2007–2018: evaluating extreme rains over hilly regions. Journal of Earth System Science
794 130:82. https://doi.org/10.1007/s12040-021-01595-1

795 Sillmann J, Kharin V v, Zhang X, others (2013) Climate extremes indices in the CMIP5
796 multimodel ensemble: Part 1. Model evaluation in the present climate. Journal of Geophysical
797 Research: Atmospheres 118:1716–1733. https://doi.org/10.1002/jgrd.50203

Singh J, Singh V, Ojha CSP (2024) Elevation dependent precipitation changes in historical and future times in the Himalayan Upper Ganga Basin, India. Atmos Res 307:107501. https://doi.org/10.1016/j.atmosres.2024.107501

Skamarock WC, Klemp JB, Dudhia J, others (2019) A description of the Advanced Research WRF model version 4. Boulder, CO

Sun Q, Miao C, Duan Q, others (2018) A review of global precipitation datasets: Data sources, estimation, and intercomparisons. Reviews of Geophysics 56:79–107. https://doi.org/10.1002/2017RG000574

Veh G, Korup O, von Specht S, others (2019) Unchanged frequency of moraine-dammed glacial lake outburst floods in the Himalaya. Nat Clim Chang 9:379–383. https://doi.org/10.1038/s41558-019-0437-5

Wester P, Mishra A, Mukherji A, Shrestha AB (eds) (2019) The Hindu Kush Himalaya Assessment: Mountains, Climate Change, Sustainability and People. Springer

Wever N, Fierz C, Mitterer C, others (2014) Solving Richards equation for snow improves snowpack meltwater runoff estimations. Cryosphere 8:257–274. https://doi.org/10.5194/tc-8-257-2014

Xu Z, Yang ZL, Tang Q, others (2021) High-resolution climate projections over Asia based on bias-corrected CMIP6 simulations. Sci Data 8:1–14. https://doi.org/10.1038/s41597-021-01079-3

Yadav M, Dimri AP, Mal S, Maharana P (2024) Elevation-dependent precipitation in the Indian Himalayan Region. Theor Appl Climatol 155:815–828. https://doi.org/10.1007/s00704-023-04661-4

Zhang MZ, Han Y, Xu Z, Guo W (2024) Assessing climate extremes in dynamical downscaling simulations driven by a novel bias-corrected CMIP6 data. Journal of Geophysical Research: Atmospheres 129:e2024JD041253. https://doi.org/10.1029/2024JD041253

Zhang X, Alexander L, Hegerl GC, others (2011) Indices for monitoring changes in extremes based on daily temperature and precipitation data. WIREs Climate Change 2:851–870. https://doi.org/10.1002/wcc.147

*Table 1. Model configuration and physical parameterization schemes used in the WRF simulations*

| Component | Scheme / Specification | Reference |
|---|---|---|
| **Model configuration** | | |
| Model | WRF-ARW v4.5.2 | Skamarock et al., 2019 |
| Domains | Two nested domains (D01, D02) | – |
| Horizontal resolution | 27 km (D01), 9 km (D02) | – |
| Grid dimension | 170 × 173 (D01), 186 × 321 (D02) | – |
| Vertical levels | 45 | – |
| Model top | 50 hPa | – |
| Simulation period | 1979–2014 | – |
| Spin-up period | 1979–1984 | – |
| Boundary conditions | Bias-corrected CMIP6 (MPI-ESM-HR) | Xu et al., 2021 |
| Boundary update frequency | 6-hourly | – |
| Nesting approach | One-way nesting | – |
| **Physical parameterization schemes** | | |
| Microphysics | Morrison double-moment scheme | Morrison et al., 2009 |
| Cumulus parameterization | Kain–Fritsch scheme (D01 only) | Kain, 2004 |
| Shortwave radiation | RRTMG scheme | Iacono et al., 2008 |
| Longwave radiation | RRTMG scheme | Iacono et al., 2008 |
| Planetary boundary layer | Yonsei University (YSU) scheme | Hong et al., 2006 |
| Surface layer | MM5 similarity scheme | Paulson, 1970 |
| Land surface model | Noah land surface model | Chen and Dudhia, 2001 |

*Table 2. Statistical metrics used for model evaluation of WRF simulations*

| S. No. | Metric | Formula |
|---|---|---|
| 1 | Mean Bias | $Bias = X_{WRF} - X_{ref}$ |
| 2 | RMSE | $RMSE = \sqrt{\frac{\sum_{i=1}^{n}\left(X_{WRF,i} - X_{ref},i\right)^2}{n}}$ |
| 3 | Spatial Correlation | $r = \frac{\sum(X_{WRF} - \overline{X}_{WRF})\,(X_{ref} - \overline{X}_{ref})}{\sqrt{\sum(X_{WRF} - \overline{X}_{WRF})^2 \sum(X_{ref} - \overline{X}_{ref})^2}}$ |

*Table 3. Statistical evaluation of WRF precipitation climatology against APHRODITE precipitation dataset during 1985–2014*

| Season | Mean Bias (mm/day) | RMSE (mm/day) | Spatial Correlation |
|---|---|---|---|
| **Annual** | +0.23 | 1.52 | 0.71 |
| **JJAS** | −0.06 | 2.83 | 0.78 |
| **DJF** | +0.37 | 1.10 | 0.65 |

*Table 4: Statistical evaluation of WRF temperature against IMDAA during1980-2014*

| Season | Mean Bias (°C) | RMSE (°C) | Spatial Correlation |
|---|---|---|---|
| **Annual** | +0.12 | 2.65 | 0.98 |
| **JJAS** | −0.66 | 2.92 | 0.98 |
| **DJF** | +0.88 | 3.03 | 0.98 |

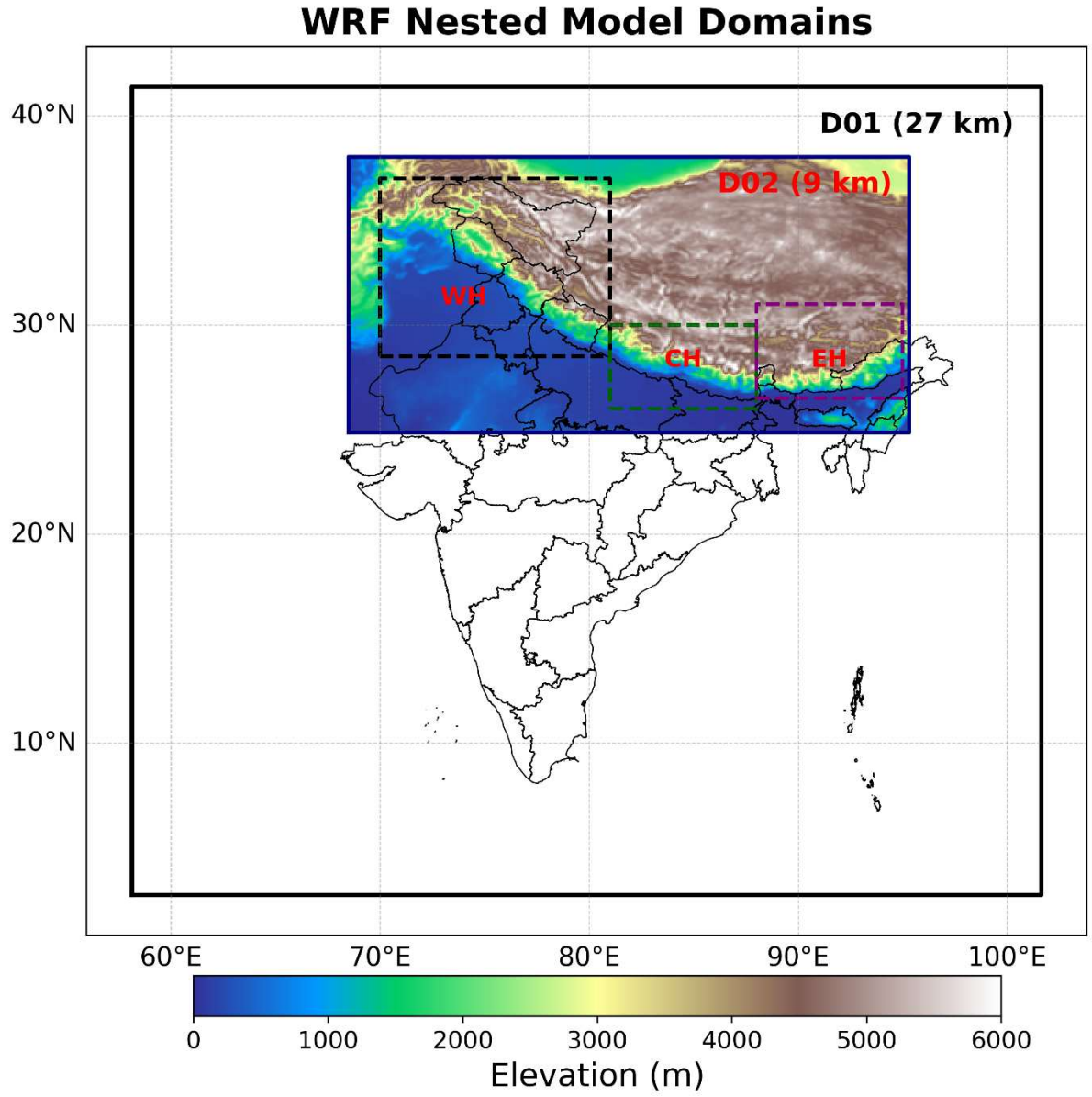


***Figure 1.*** *WRF nested model domains (D01: 27 km; D02: 9 km) and the Himalayan study regions used in the analysis: Western Himalaya (WH), Central Himalaya (CH), and Eastern Himalaya (EH). Background shading shows elevation (m).*

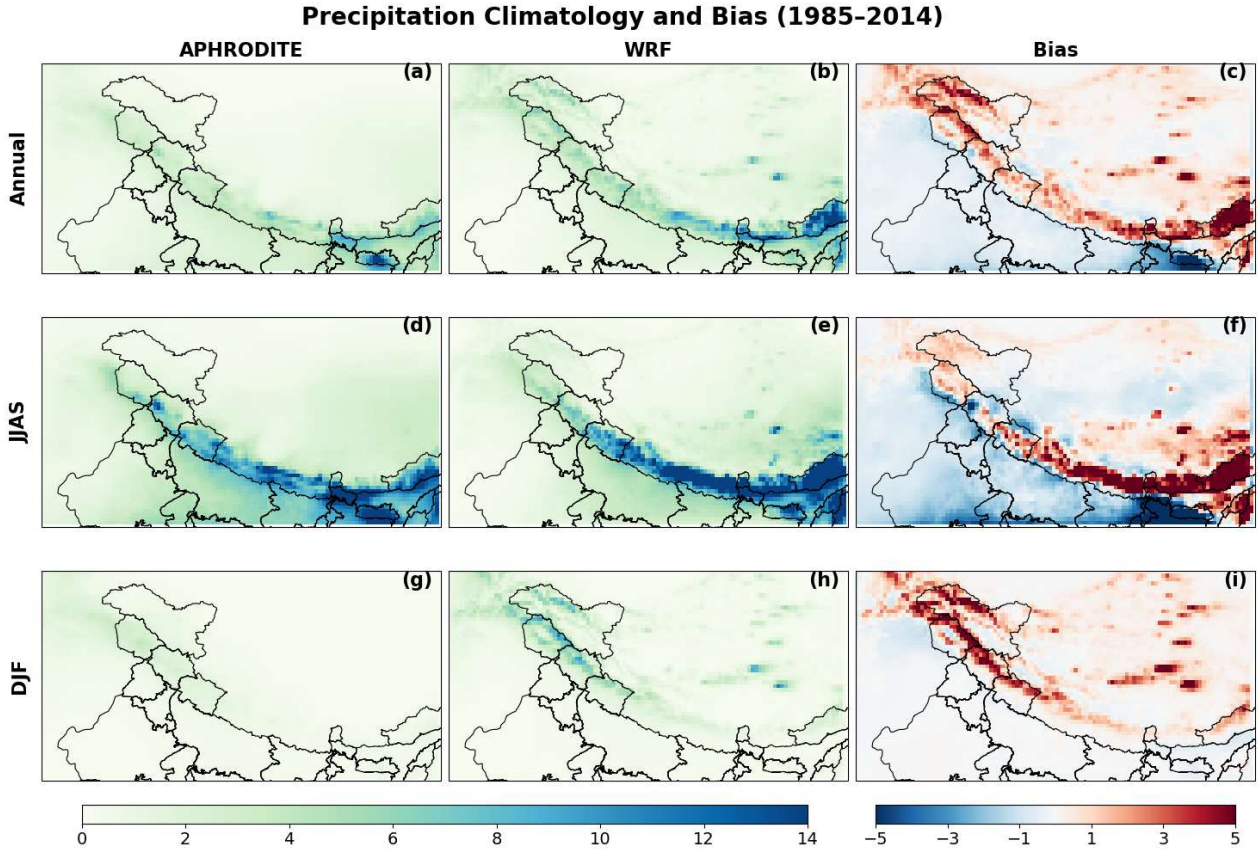


***Figure 2***. *Annual mean precipitation climatology (mm day$^{-1}$) over the Himalayan region for 1985–2014. Panels (a–c) show annual precipitation from APHRODITE, WRF, and their bias (WRF − APHRODITE), respectively. Panels (d–f) and (g–i) show corresponding results for the JJAS monsoon and DJF winter seasons.*

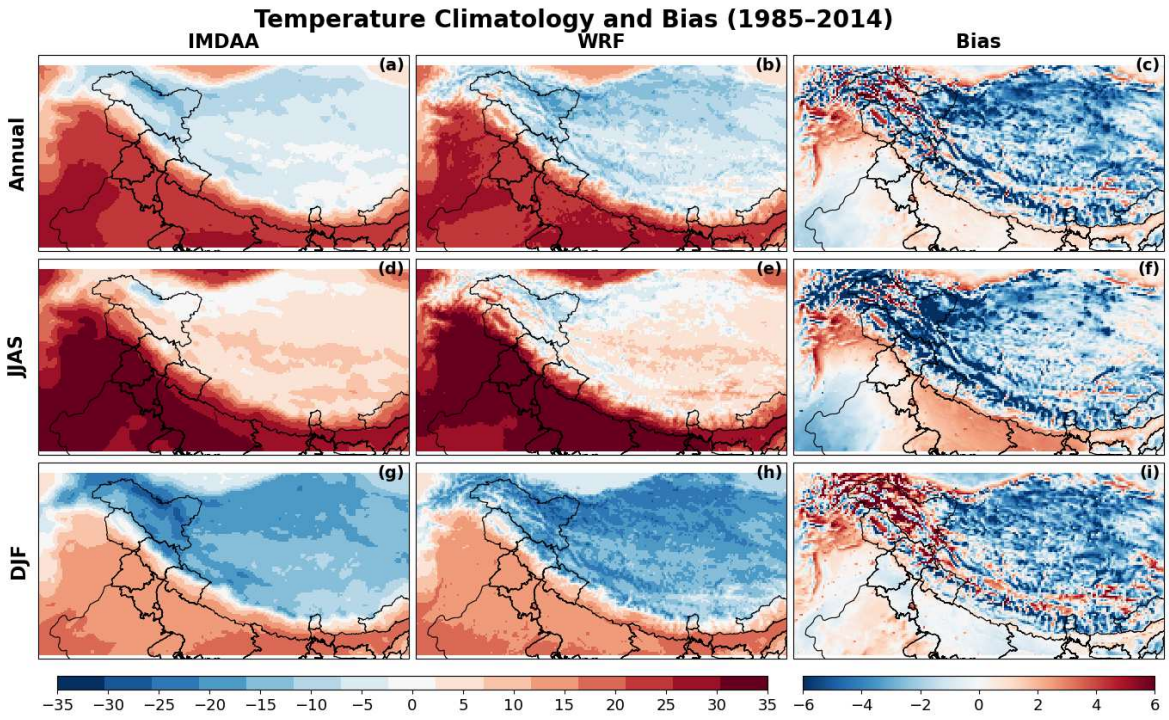


***Figure 3.*** *Mean near-surface air temperature climatology (°C) over the Himalayan region during 1985–2014 from the IMDAA reanalysis and WRF simulations. Panels (a–c) show annual mean temperature from IMDAA, WRF, and their bias (WRF − IMDAA), respectively. Panels (d–f) and (g–i) show corresponding results for the JJAS (monsoon) and DJF (winter) seasons.*

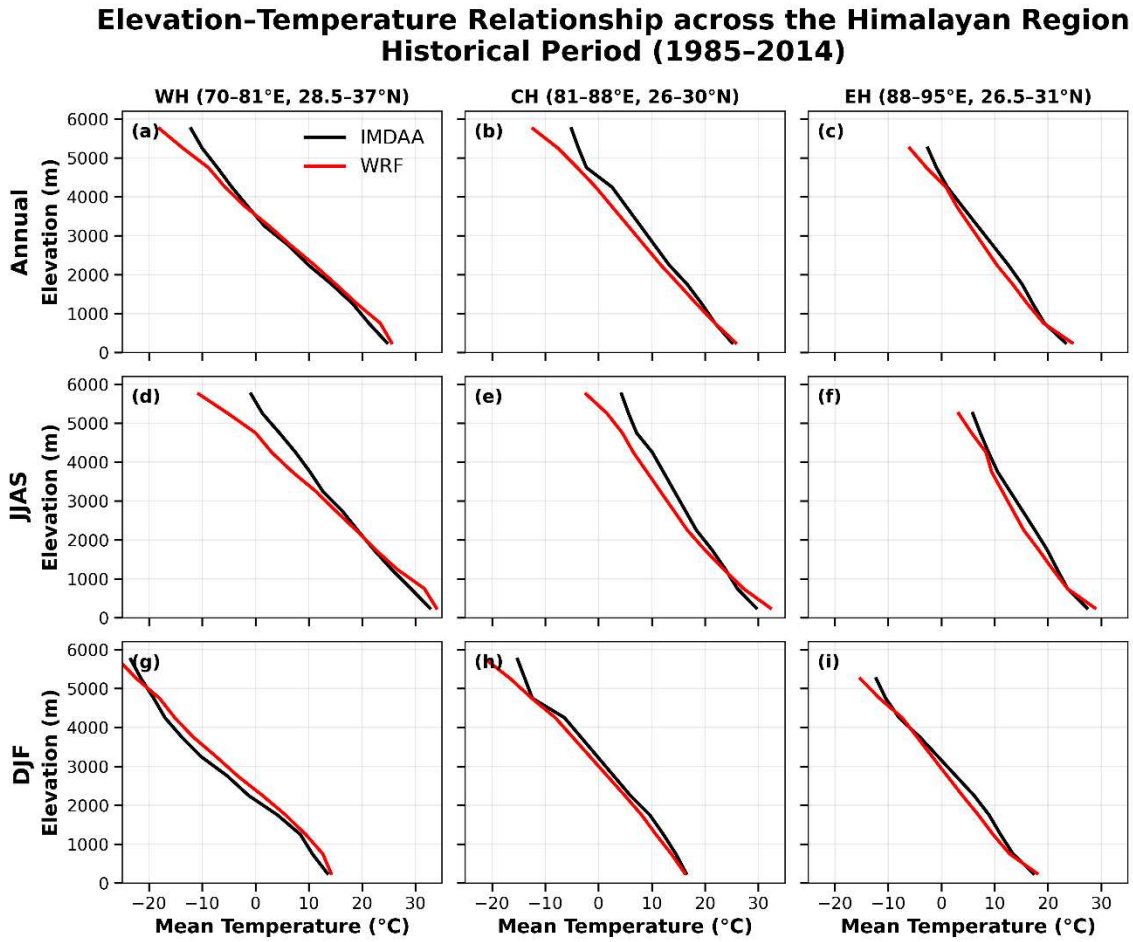


***Figure 4.*** *Elevation–temperature relationship derived from IMDAA and WRF simulations across the Western Himalaya (WH: 70–81°E, 28.5–37°N), Central Himalaya (CH: 81–88°E, 26–30°N), and Eastern Himalaya (EH: 88–95°E, 26.5–31°N) during 1985–2014. Panels (a–c), (d–f), and (g–i) represent annual, JJAS, and DJF temperature–elevation relationships, respectively.*

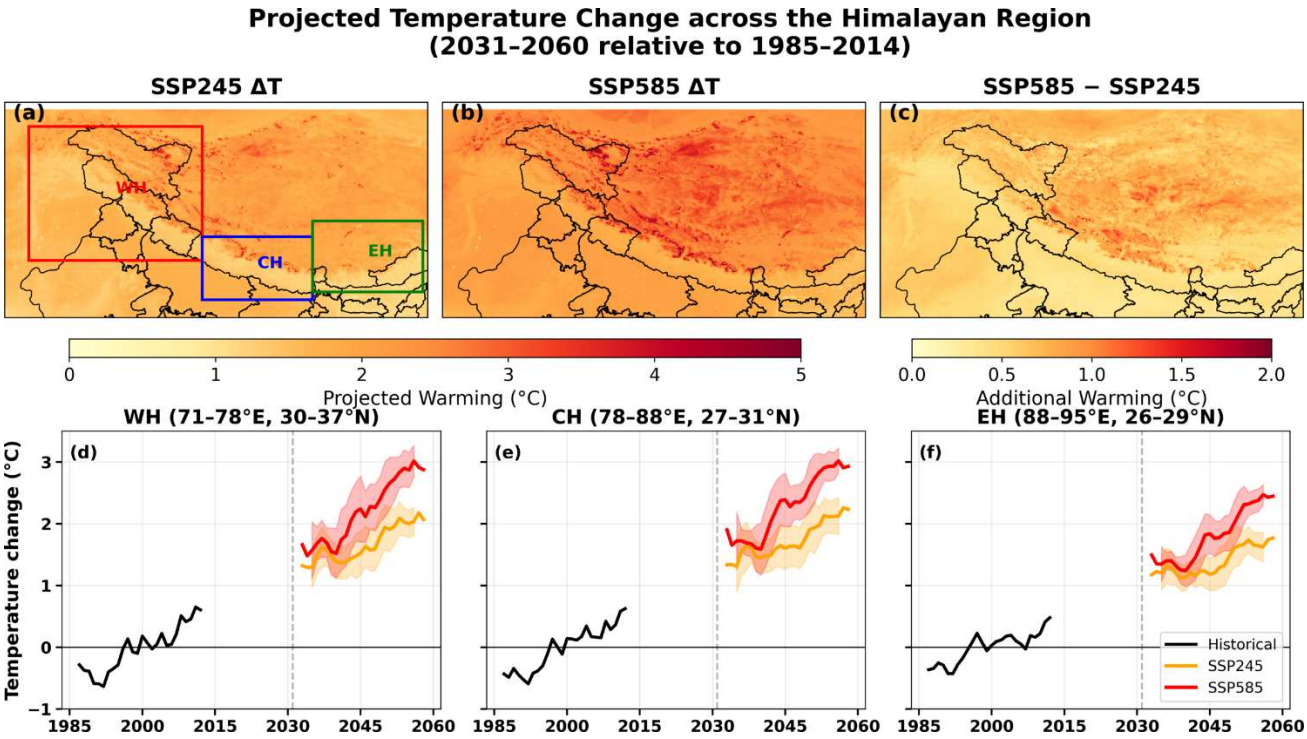


***Figure 5.*** *Projected temperature change over the Himalayan region from dynamically downscaled WRF simulations forced by CMIP6 scenarios. (a) Warming relative to the historical baseline (1985–2014) under SSP2-4.5. (b) Warming relative to the historical baseline under SSP5-8.5.* ***(c)*** *Additional warming (SSP5-8.5 − SSP2-4.5).* ***(d–f)*** *Regional mean temperature anomalies for the Western (WH), Central (CH), and Eastern Himalaya (EH). Curves show 5-year running means and shaded bands represent variability estimated using a 9-year rolling standard deviation.*

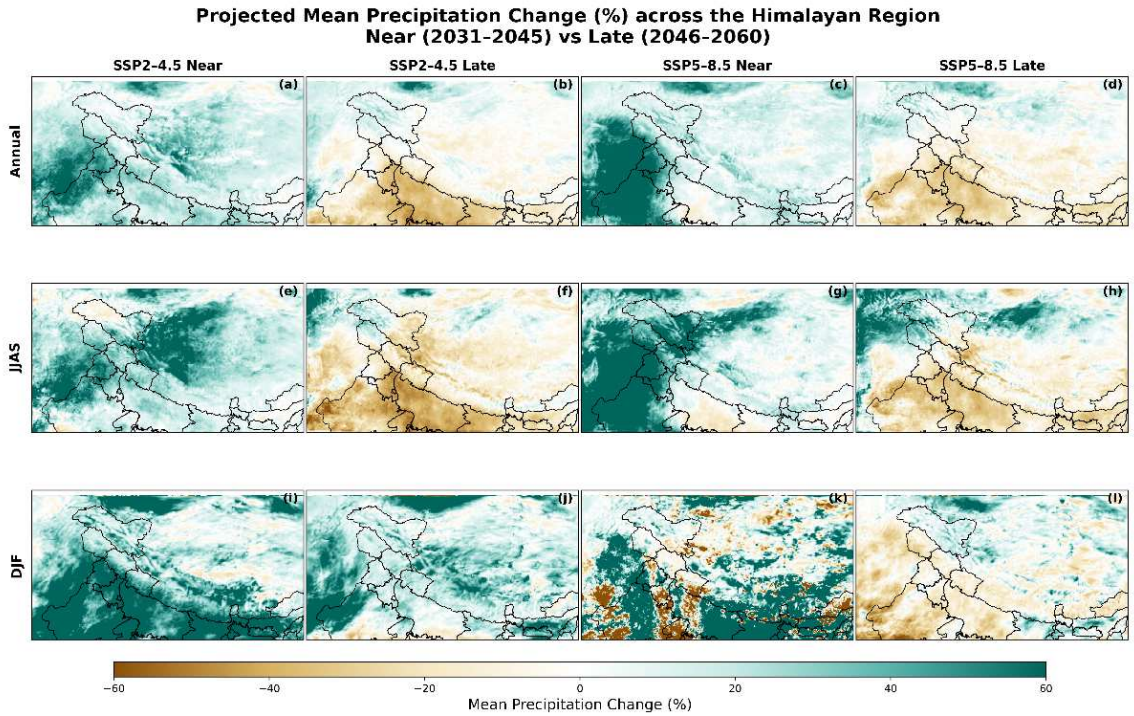


***Figure 6A.*** *Spatial distribution of projected mean precipitation change (%) over the Himalayan region for the near-future (2031–2045) and late-future (2046–2060) periods relative to the historical baseline period (1985–2014). Rows correspond to (a–d) annual, (e–h) JJAS (monsoon), and (i–l) DJF (winter) seasons, while columns represent SSP2–4.5 near, SSP2–4.5 late, SSP5–8.5 near, and SSP5–8.5 late scenarios, respectively. Percentage changes are computed from seasonal mean precipitation (mm day$^{-1}$).*

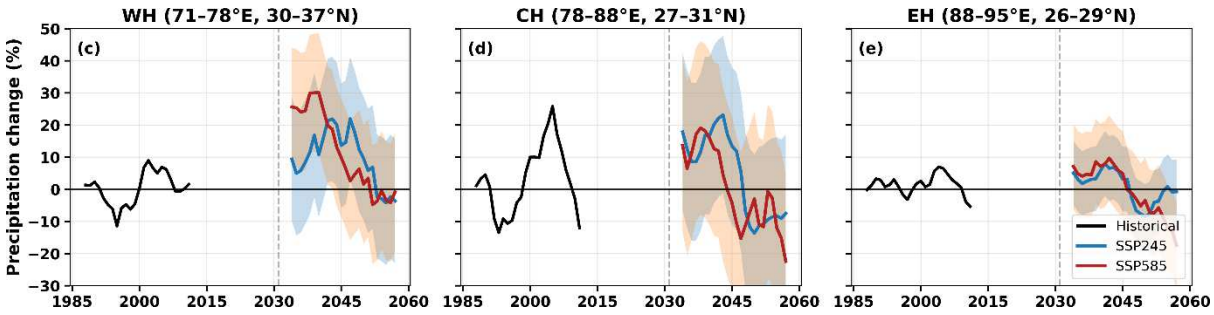


***Figure 6B.*** *Temporal evolution of annual mean precipitation change (%) relative to the historical baseline period (1985–2014) for the Western Himalaya (WH), Central Himalaya (CH), and Eastern Himalaya (EH). Solid lines represent 7-year running mean anomalies derived from WRF simulations for the historical period and future projections under SSP2–4.5 and SSP5–8.5 (2031–2060). Shaded bands represent variability estimated using the standard deviation of projected anomalies. The vertical dashed line marks the transition to the projection period (2031).*

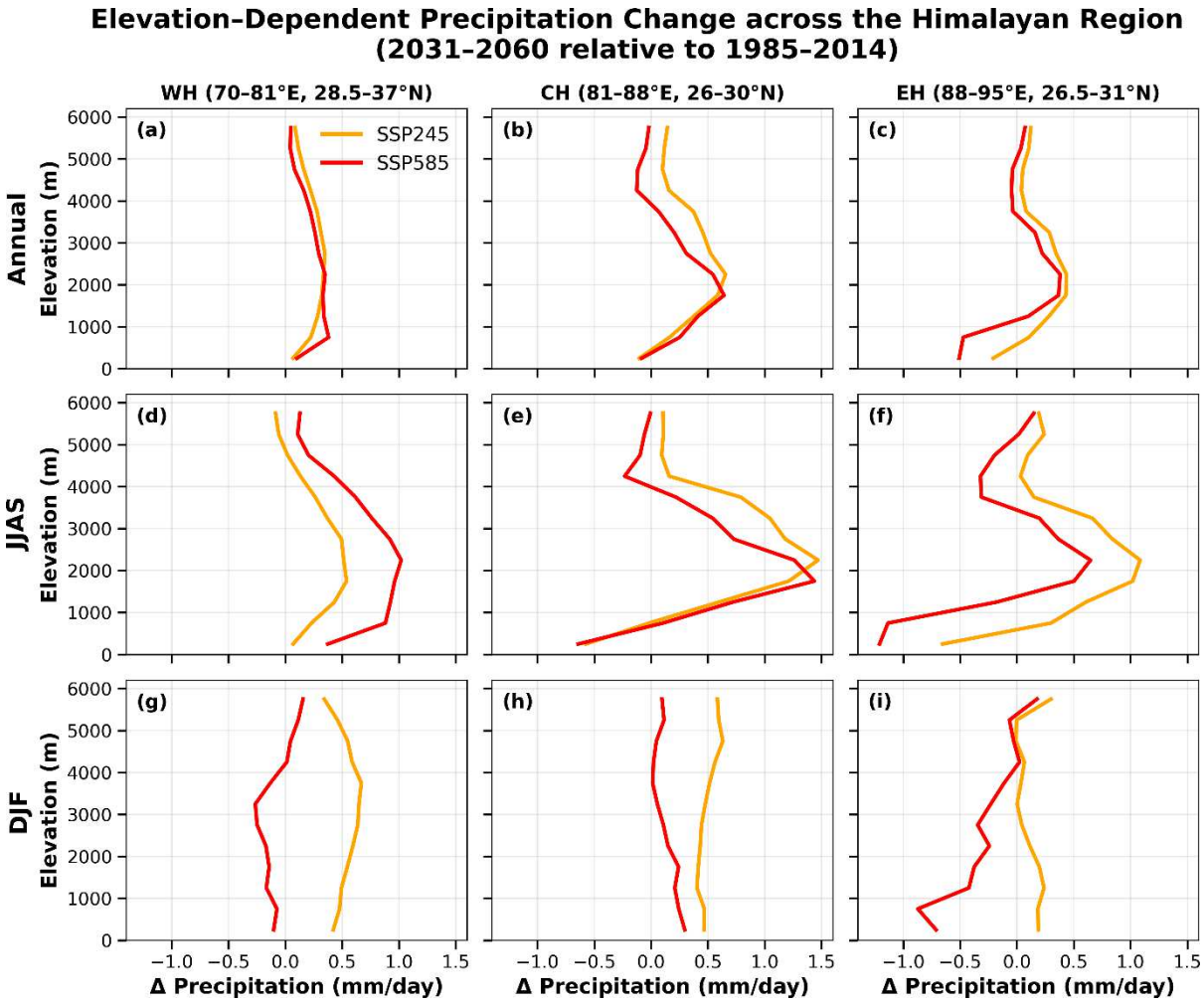


***Figure 7.*** *Elevation-dependent changes in mean precipitation (ΔP; mm day⁻¹) across the Himalayan region for the mid-21st century period (2031–2060) relative to the historical baseline period (1985–2014). Columns represent the Western Himalaya (WH), Central Himalaya (CH), and Eastern Himalaya (EH), while rows correspond to (a–c) annual, (d–f) JJAS (monsoon), and (g–i) DJF (winter) seasons. Orange and red lines denote SSP2–4.5 and SSP5–8.5, respectively. Profiles are computed using 500 m elevation bins and include only grid points with baseline precipitation ≥1 mm day⁻¹. Positive (negative) values indicate increased (decreased) precipitation intensity.*

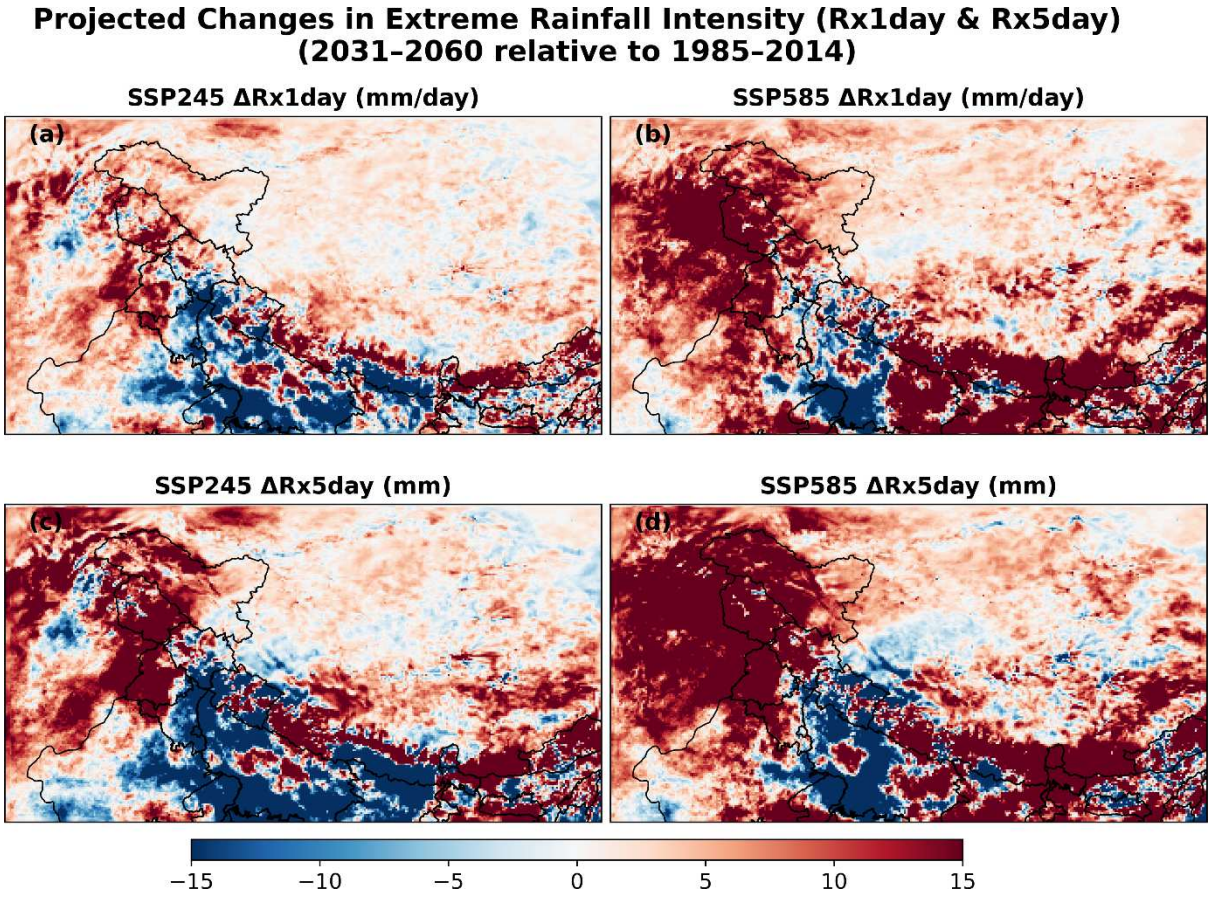


***Figure 8.*** *Projected changes in extreme precipitation intensity across the Himalayan region for 2031–2060 relative to the historical baseline period (1985–2014). Panels (a) and (b) show changes in annual maximum 1-day precipitation (Rx1day; mm day$^{-1}$) under SSP2–4.5 and SSP5–8.5, respectively, while panels (c) and (d) show corresponding changes in maximum consecutive 5-day precipitation (Rx5day; total, mm). Extreme indices are computed annual maxima of daily precipitation (Rx1day) and consecutive 5-day precipitation (Rx5day). Positive values indicate intensification of extreme events.*

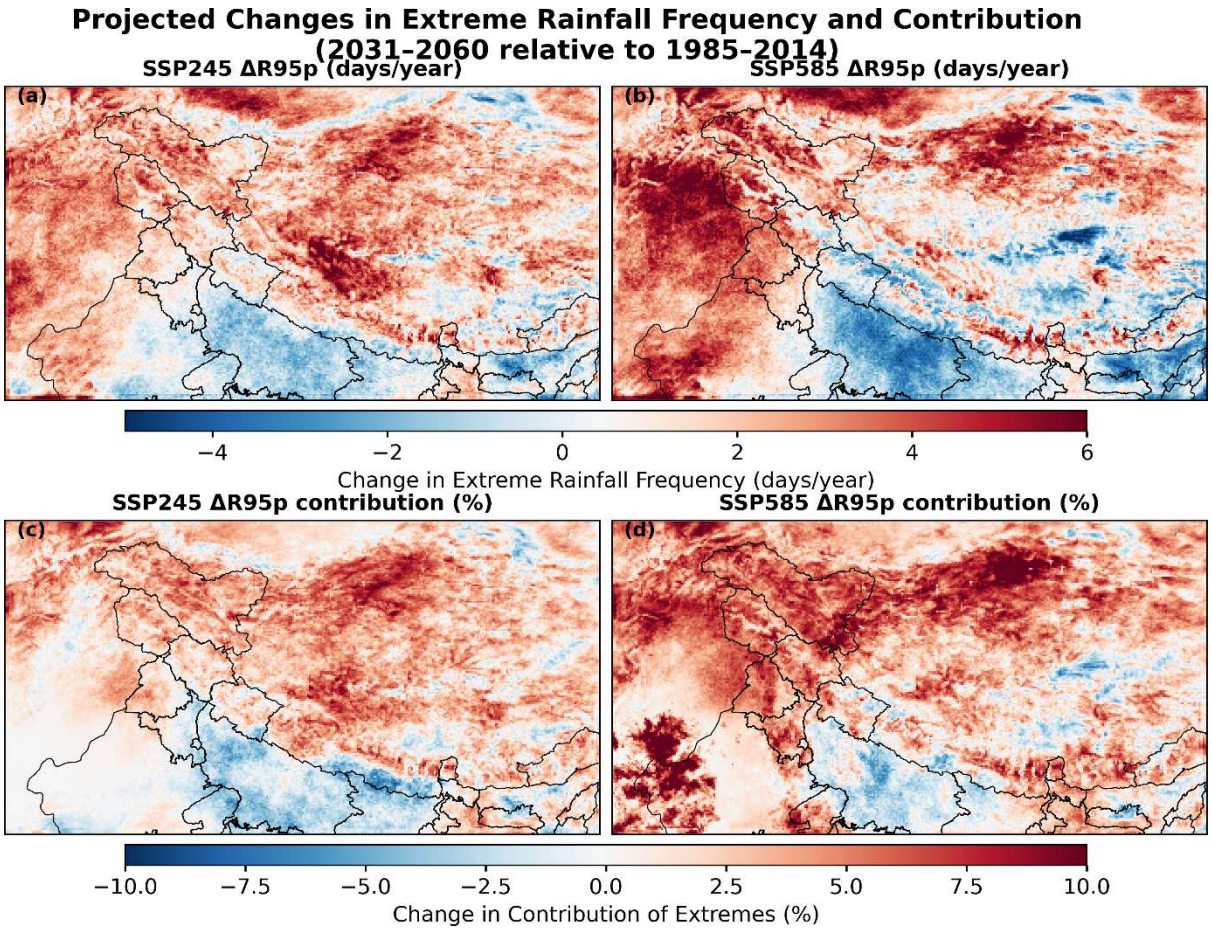


***Figure 9.*** *Spatial distribution of projected changes in extreme precipitation across the Himalayan region for 2031–2060 relative to the historical baseline period (1985–2014). Panels (a) and (b) show changes in the frequency of extreme precipitation events (R95p; days yr$^{-1}$) under SSP2–4.5 and SSP5–8.5, respectively, while panels (c) and (d) show corresponding changes in the contribution of extreme precipitation (R95p) to total rainfall (%). Extremes are defined using the 95th percentile of wet-day precipitation (≥1 mm day$^{-1}$) from the historical period. Positive values indicate an increase in either occurrence or contribution.*

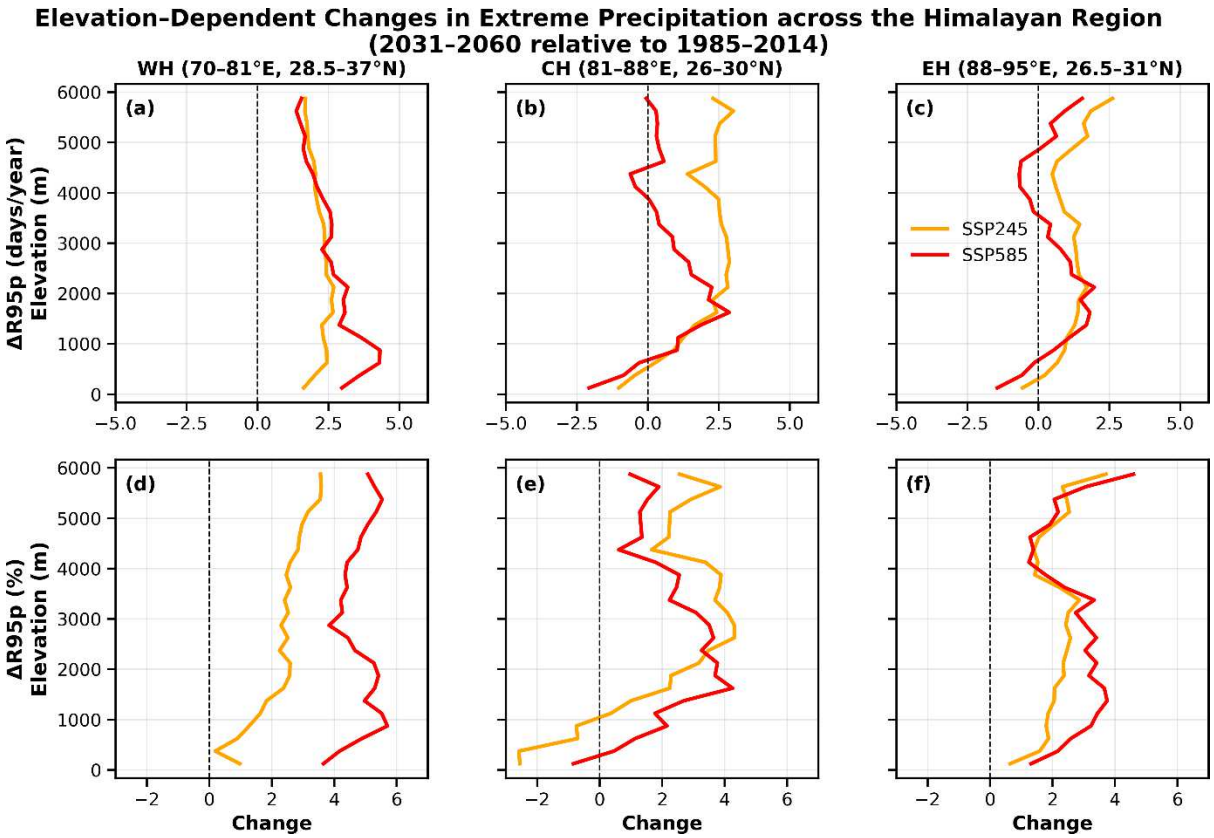


***Figure 10.*** *Elevation-dependent changes in extreme precipitation across the Himalayan region for 2031–2060 relative to the historical baseline period (1985–2014). Panels (a–c) show changes in the frequency of extreme precipitation events (R95p; days yr$^{-1}$) for WH, CH, and EH, respectively, while panels (d–f) show corresponding changes in the contribution of extremes to total precipitation (%). Profiles are computed using 500 m elevation bins. Positive values indicate an increase relative to the historical period.*

## Supplementary Files

This is a list of supplementary files associated with this preprint. Click to download.

- supplementaryfigures.docx